IEEE Access
Multidisciplinary | Rapid Review | Open Access Journal

Received May 1, 2019, accepted May 20, 2019, date of publication May 23, 2019, date of current version June 4, 2019.

Digital Object Identifier 10.1109/ACCESS.2019.2918556

Hotspot Temperature Monitoring of Fully Insulated Busbar Taped Joint

LIEZHENG TANG[1], (Student Member, IEEE), JIANGJUN RUAN[1], (Member, IEEE), ZHIFEI YANG[1], ROU CHEN[2], GUANNAN LI[1], AND XUEFENG YIN[1]

[1]School of Electrical Engineering and Automation, Wuhan University, Wuhan 430072, China
[2]China Electric Power Research Institute Co., Ltd., Wuhan 430000, China

Corresponding author: Liezheng Tang (tlz9302@163.com)

ABSTRACT The fully insulated busbar has been extensively used in power and shipboard applications due to its favorable economic efficiency and excellent performance. Because of contact resistance and larger insulation thermal resistance, the joint, in certain circumstances, form a hotspot in the circuit. For hotspot temperature monitoring, therefore, this paper proposed an indirect approach which consists of radial direction temperature calculation (RDTC) in the busbar and axial direction temperature calculation (ADTC) in the conductor. The RDTC is to calculate the conductor temperatures from the surface temperatures of busbar in two different spots near the joint through the transient thermal network. The ADTC is to estimate the hotspot temperature from the conductor temperatures obtained in the RDTC using a fitted functional expression. The influence of solar radiation on the temperature distribution is greatly reduced by averaging the surface temperature in the RDTC and adjusting the functional form in the ADTC. A temperature-rise test on a practical insulated busbar taped joint was performed outdoors in hot summer to validate this approach. The calculated hotspot temperature agrees well with the measured result with a maximum error of only 3.8 K, indicating the high model precision and strong robustness to the solar radiation impact. Some factors in the applications of temperature monitoring are also discussed. This method is expected to be applied to the engineering application, thus improving the condition monitoring of the fully insulated busbar.

INDEX TERMS Fully insulated busbar taped joint, solar radiation, temperature monitoring, transient thermal network, thermal analysis.

I. INTRODUCTION

The solid insulated busbar, commercially available mainly in Europe [1]–[3], is normally intended for the electrical connections of power equipment with rated current from several to over 10 kA. In power utility and shipboard applications, the solid insulated busbar offers many advantages over conventional cable or gas insulated busbar, such as high ampacity, excellent dielectric property, compact dimension with reduced bending radius and so on [4]–[6]. Therefore, this product has been widely used around the world, such as Austria, Switzerland, Japan, USA and especially China, where the total length of the solid insulated busbar up to 35 kV was nearly 200 km in 2014 for various applications [2], [4], [7]–[9].

In terms of the insulation modes, solid insulated busbars can be categorized into two types, namely fully insulated busbar and partially insulated busbar [10], [11]. The former one is fully electrically shielded by the use of earth screen and thus touch safe throughout the whole length under operational conditions. On the other hand, the conductor in the partially insulated busbar is only covered by a layer of oversheath with no earth screen so that it is not fully grounded for personnel safety. Similar to the power cable, a fully insulated busbar consists primarily of the current-carrying conductor, tubular insulating layer and earth screen as well as oversheath [12]. But for a fully insulated busbar, the conductor is a hollow conductor rather than stranded conductors, and conductive layers are embedded in the insulation to reach an optimized electric field distribution at the busbar ends [4].

The length of the individual busbar is limited by the manufacturing process, transportation as well as installation conditions and usually no more than 10 meters. Hence, most of the practical solid insulated busbar routes consist of dozens or even hundreds of single busbar segments connected in series through joints. According to the assembly methods, there are

The associate editor coordinating the review of this manuscript and approving it for publication was Amedeo Andreotti.

mainly two types of joints, including prefabricated type and taped type. The key element of prefabricated joint is the fully insulated connecting sleeve, inside which there are capacitive gradings and earth layer to guarantee a homogenous electric field inside the joint [9]. As for the taped joints, the semi-conducting and the insulating tapes are wounded around the busbar to form the conductor screen and the insulation layer [13], [14].

Although the solid insulated busbar has been commercially available in Europe for more than half a century, its wide application in China and USA has emerged since the late 2000s. Owing to lack of industry standards and operational experience, more and more faults caused by poor insulation design, manufacturing defects, overheating and moisture ingress have been reported recently in China [11], [15]–[19]. Based on the above background, lots of Chinese scholars have carried out a preliminary study on the condition monitoring and fault diagnostic for solid insulated busbar. The current researches mostly focus on the partial discharge detection [20]–[24], electric field simulation of defective busbar [25], [26], and thermal ageing [7], [27].

In fact, the joint would probably form a hot spot of the solid insulated busbar circuit due to unqualified design or assembly [14], which accelerates the thermal ageing and shortens its insulation lifetime. Therefore, it is necessary to measure the temperature inside the joint. However, the direct conductor temperature measurement is technically difficult to perform because of the high potential in the conductor. As a result, the indirect approach is the only feasible way for on-line temperature monitoring of the joint. Since the surface temperature needs to be measured through the temperature sensor in the indirect method, only the fully insulated busbar is considered for security in this paper.

However, there is almost no reported literature regarding the temperature monitoring of the fully insulated busbar joint. Fortunately, the fully insulated busbar is considerably similar in structure to the power cable, of which the temperature monitoring for the joint from cable surface temperatures is basically achieved [28]. The main difference between them lies in that the busbar may be installed outdoors and the temperature profile will be easily affected by the solar heating. It could be expected that indiscriminately imitating the method utilized in cable joint will lead to a large temperature error for the fully insulated busbar joint. For this reason, taking the taped joint as an example, this paper puts forward an approach for monitoring the hotspot temperature inside the fully insulated busbar joint, which could effectively overcome the thermal impact of the solar radiation.

II. METHODOLOGY

For better understanding of the temperature monitoring method, it is necessary to analyze the heat flux distribution within the insulated busbar taped joint. As seen in Fig. 1, due to the high thermal conductivity of the conductor, most of the heat flux will be transported in the conductor from connector to both sides. Meanwhile, in the radial direction of the busbar, the heat will be transferred from the hot conductor to the cold surface. Based on the above principle, the hotspot temperature could be estimated along the radial and axial heat fluxes mentioned above from the surface temperatures.

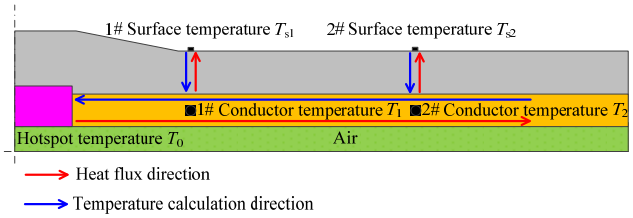

FIGURE 1. A conceptual diagram of the temperature monitoring for an insulated busbar joint.

The first step is to calculate the conductor temperatures (T_1, T_2) using the surface temperatures (T_{s1}, T_{s2}) in two different axial positions along the radial heat flux. Subsequently, the obtained conductor temperatures (T_1, T_2) in the busbar can be adopted to estimate the hotspot temperatureT_0 inside the joint in the axial direction. The former step is named as radial direction temperature calculation RDTC) in the busbar while the latter one is called axial direction temperature calculation (ADTC) in the conductor. In this approach, the inputs that need to be measured contain two surface temperatures and current.

A. RDTC

1) TRANSIENT THERMAL NETWORK OF THE INSULATED BUSBAR

The typical structure of the 10 kV insulated busbar is illustrated in Fig. 2, where the insulation consists of two parts, Polytetrafluoroethylene (PTFE) layer and Cross-linked polyethylene (XLPE) layer. The structural and thermal parameters of the busbar are given in Table 1 [29]–[31], where the thermal properties of air are approximated by linear functions with temperature ranging from 273 to 363 K considering their temperature dependences [32].

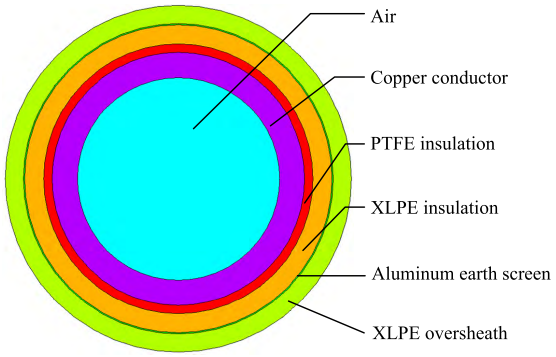

FIGURE 2. The structure of the 10 kV insulated busbar.

Due to the similarity between the cable and fully insulated busbar, the conductor temperature in the fully insulated busbar can be calculated through a 1-D transient thermal

TABLE 1. The structural and thermal parameters of the insulated busbar.

Components	Outer radius (mm)	Thermal conductivity (W/(m·K))	Volumetric specific heat (kJ/(m^3·K))
Air	26	$0.0036+7.346\times10^{-5}T$	$2.267-0.00359T$
Copper conductor	30	383	3450
PTFE insulation	32	0.259	2290
XLPE insulation	36.5	0.286	2400
Aluminum earth screen	36.8	218	2500
XLPE oversheath	40.1	0.286	2400

network from the surface temperature. The major difference in their structures lies in that there is internal air inside the hollow conductor of the busbar involving both heat conduction and convective heat transfer. Due to the closed ends of the busbar, the convective heat transfer is natural convection, where any fluid motion occurs by buoyancy. Since the Copper conductor is nearly isothermal and the air thermal diffusivity is quite large due to its extremely low density, the temperature gradient of internal air is considerably small. Accordingly, the convective heat transfer can be almost neglected due to the low temperature gradient. As for the heat conduction, the thermal resistance of internal air can be ignored due to the isothermal inner surface of Copper conductor while the thermal capacitance of the air is also negligible because of its considerably low density. That is to say, not only the convective heat transfer but also the heat conduction of the internal air can be ignored in the thermal analysis. To verify the above analysis, two 2-D transient thermal analyses on the fully insulated busbar are carried out. One of the models sets the air inside the conductor as a fluid while the other one does not build the air region in the model involving only heat conduction. It is found that conductor temperatures obtained using two models are pretty close to each other with maximum temperature difference less than 0.3 K. Apparently, the internal air can be completely neglected in the thermal network of the busbar.

The other layers can be easily represented by lumped π-type *RC* thermal circuit branches as per IEC 60853 [29] and thus the transient thermal network is provided in Fig. 3.

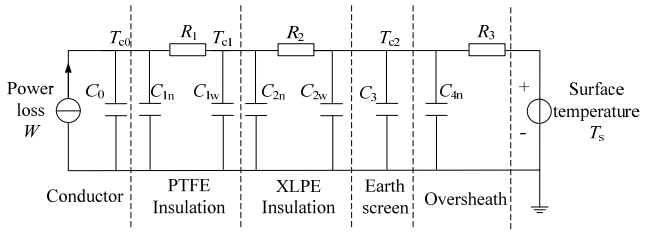

FIGURE 3. Transient thermal network of the insulated busbar.

For each layer, the thermal resistance per unit length is calculated as

$$R_i = \frac{\ln(\frac{r_i}{r_{i-1}})}{2\pi\lambda_i} \tag{1}$$

where λ_i is the thermal conductivity of *i*th layer. r_{i-1} and r_i are the inner and outer radius of *i*th layer.

The thermal capacitance is allocated at inner and outer side of each layer as follows [29]

$$\begin{aligned} C_{in} &= p_i C_i \\ C_{iw} &= (1-p_i)\, C_i \\ C_i &= c\pi(r_i^2 - r_{i-1}^2) \\ p_i &= \frac{1}{2\ln\left(\frac{r_i}{r_{i-1}}\right)} - \frac{1}{\left(\frac{r_i}{r_{i-1}}\right)^2 - 1} \end{aligned} \tag{2}$$

where c is the volumetric specific heat and C_i is the total thermal capacitance per unit length of *i*th layer.

Based on formula (1), (2) and Table 1, the lumped thermal resistances and capacitances per unit length of the insulated busbar from Fig. 3 can be calculated as Table 2.

TABLE 2. The thermal resistances and capacitances per unit length of insulated busbar.

Parameters	R_1(K/(W·m))	R_2(K/(W·m))	R_3(K/(W·m))	C_0(K/(W·m))	C_{1n}(K/(W·m))
Values	0.0397	0.0732	0.0478	2428	436
Parameters	C_{1w}(J/(W·m))	C_{2n}(J/(W·m))	C_{2w}(J/(W·m))	C_3(J/(W·m))	C_{4n}(J/(W·m))
Values	456	1111	1213	457	929

In practical application, both the load current and the surface temperature change over time. Hence, the first step for solving the thermal network is to approximate these continuous variables by a series of single-step functions with the step size of 1 min in this paper. In each substep, the conductor temperature can be obtained by calculating the single-step response where the initial temperatures of each layer are the corresponding temperatures in the last moment of the previous substep.

Based on the theory of dynamic circuit, the single-step response can be solved by state variable analysis. As per Kirchhoff's law, the state equations can be written as

$$\begin{cases} (C_0 + C_{1n})\dfrac{dT_{c0}}{dt} + \dfrac{T_{c0} - T_{c1}}{R_1} - W = 0 \\ \dfrac{T_{c0} - T_{c1}}{R_1} + \dfrac{T_{c2} - T_{c1}}{R_2} - (C_{1w} + C_{2n})\dfrac{dT_{c1}}{dt} = 0 \\ \dfrac{T_{c1} - T_{c2}}{R_2} + \dfrac{T_s - T_{c2}}{R_3} - (C_{2w} + C_3 + C_{4n})\dfrac{dT_{c2}}{dt} = 0 \end{cases} \tag{3}$$

Putting the above equations in the standard form leads to

$$\begin{bmatrix} \frac{dT_{c0}}{dt} \\ \frac{dT_{c1}}{dt} \\ \frac{dT_{c2}}{dt} \end{bmatrix} = \begin{bmatrix} \frac{-1}{R_1(C_0+C_{1n})} & \frac{1}{R_1(C_0+C_{1n})} & 0 \\ \frac{1}{R_1(C_{1w}+C_{2n})} & \frac{-(R_1+R_2)}{R_1R_2(C_{1w}+C_{2n})} & \frac{1}{R_2(C_{1w}+C_{2n})} \\ 0 & \frac{1}{R_2(C_{2w}+C_3+C_{4n})} & \frac{-(R_2+R_3)}{R_2R_3(C_{2w}+C_3+C_{4n})} \end{bmatrix} \times \begin{bmatrix} T_{c0} \\ T_{c1} \\ T_{c2} \end{bmatrix} + \begin{bmatrix} \frac{1}{C_0+C_{1n}} & 0 \\ 0 & 0 \\ 0 & R_3(C_{2w}+C_3+C_{4n}) \end{bmatrix} \begin{bmatrix} W \\ T_s \end{bmatrix} \tag{4}$$

The standard way to represent the state equations is to arrange them as a set of first-order differential equations

$$\dot{\boldsymbol{X}} = \boldsymbol{AX} + \boldsymbol{BU}, \quad \boldsymbol{X}(0_-) = \boldsymbol{X}_0 \tag{5}$$

where $\boldsymbol{X}=[T_{c0}\ T_{c1}\ T_{c2}]^T$ is the state vector and the dot represents the first derivative with respect to time. $\boldsymbol{U}$ is the input vector. $\boldsymbol{A}$ and $\boldsymbol{B}$ are respectively 3×3 and 3×2 matrices.

By taking the Laplace transform, equation (5) can be arranged as

$$\boldsymbol{X}(s) = [s\boldsymbol{I} - \boldsymbol{A}]^{-1}(\boldsymbol{X}_0 + \boldsymbol{BU}(s)) \tag{6}$$

where $\boldsymbol{I}$ is the identity matrix.

After the inverse Laplace transform of the equation (6), the state vector can be obtained. Step by step, the conductor temperatures over time can be calculated. Because of the matrix computation and Laplace transform involved, MATLAB was adopted to solve the equations in this paper.

2) THE EFFECT OF SOLAR RADIATION ON RDTC

As mentioned in Introduction section, the main difference between power cable and insulated busbar is that the latter is assembled outdoors and thus directly exposed to the solar radiation. This radiation will increase the overall temperature of the busbar and also result in the uneven surface temperature, which may lower the precision of thermal network. Hence, the impact of solar radiation on RDTC is discussed and examined in this part by comparison of the calculated temperature based on transient thermal network and finite element method (FEM).

Firstly, FEM-based transient thermal analysis is carried out to obtain the temperature rise, which can be deemed as the theoretical value. Actually, it is difficult to accurately take into account the solar radiation. Because the solar power absorbed by an object is time-varying and strongly dependent on its spatial location, direction of placement, surface nature and even the weather conditions. Nevertheless, since the main attention of this part is drawn to the solar radiation effect rather than the actual conductor temperature in practical situations, this problem can be greatly simplified.

As per IEC 60287 [33], the intensity of solar radiation should be taken as 1000 W/m^2 for most latitudes, and the solar absorptivity of the busbar surface α is set to 0.4 for XLPE oversheath. In fact, the solar radiation changes over time in the daytime. Considering the time dependence of the solar radiation, it is reasonable to assume that the solar heat flux varies sinusoidally with time from sunrise to sunset as follows

$$q = 1000 \sin\left(\frac{2\pi t}{24}\right) W/m^2 \tag{7}$$

Create a Cartesian coordinate system with the origin located in the center of the busbar as shown in Fig. 4. X-axis is defined to be perpendicular to the sunlight while Y-axis points to the sun. θ is defined as the angle between X-axis and the line connecting the surface point and origin. Then, the solar heat flux absorbed by the surface point with any angle of θ is expressed as

$$q_s = \alpha q \sin(\theta) \tag{8}$$

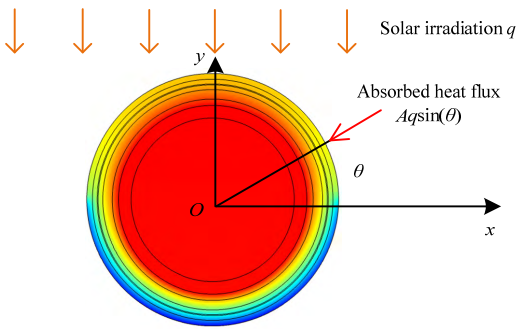

FIGURE 4. The schematic diagram of the busbar absorbing the solar radiation.

The ambient temperatureand the initial temperatureof the insulated busbar are all set to 25°. When t>0, a load current of 1300 A is injected into the conductor and the busbar is exposed to the sun at the same time.

As the lower surface of the busbar does not involve solar radiation, this boundary typically satisfies combined convection and radiation condition, which can be as [32]

$$-\lambda\frac{\partial T}{\partial n} = h(T_\infty - T) + \varepsilon\sigma(T_\infty^4 - T^4) \tag{9}$$

where T_∞ and T are the ambient temperature and surface temperature, respectively. h is the convection heat transfer coefficient and ε is the emissivity of the surface, usually set to 0.95 for the oversheath [34]. $\sigma = 5.67 \times 10^{-8}$ W/m^2·K^4 is the Stefan-Boltzman constant. The first term of the right side of the formula (9) represents the convective heat transfer between the surface and air while the second one is the surface-to-ambient radiation.

The convective heat transfer coefficient depends greatly on the variation of temperature and geometry of the surface as

well as its orientation and the thermophysical properties of the air. The complexities of air motion make it quite difficult to obtain simple analytical relations for convective heat transfer coefficient, but fortunately, there are some empirical correlations for the average convective heat transfer coefficient. The fully insulated busbar is representative of a horizontal cylinder, of which the convective heat transfer coefficient is expressed as [32]

$$h = \left\{0.6 + \frac{0.387\mathrm{Ra}^{1/6}}{[1 + (0.599/\mathrm{Pr})^{9/16}]^{8/27}}\right\}^2 \lambda/L \qquad (10)$$

where L is the diameter of the cylinder, m and Pr is the Prandtl number of air, almost 0.73 in the temperature range from 10 to 40° [32]. Ra is the Rayleigh number, which is

$$Ra = \frac{g\beta(T - T_\infty)L^3 \,\mathrm{Pr}}{\upsilon^2} \qquad (11)$$

where g is gravitational acceleration, nearly 10 m/s^2; β is coefficient of volume expansion, 1/K, which is equal to $1/T$ for the air; υ is the kinematic viscosity of the air, nearly 1.85×10^{-5} W/m^2·K^4 between 10 and 40° [32]. It should be noted that only if Ra is no more than 10^{12}, could the formula (10) be suitable for the horizontal cylinder.

As for the upper surface of the busbar, not only air convection combined with surface radiation but also solar radiation are involved, and the latter one can be represented by specified heat flux. Hence, the upper surface satisfies the generalized boundary conditions involving convection, radiation and specified heat flux, and can be expressed as

$$-\lambda\frac{\partial T}{\partial n} = h(T_\infty - T) + \varepsilon\sigma(T_\infty^4 - T^4) + \alpha q \sin(\theta) \qquad (12)$$

With the determined boundary conditions and power loss in the conductor, the transient temperature field can be easily solved by FEM. The obtained surface temperatures are adopted to calculate the conductor temperatures by transient thermal network while the conductor temperatures from FEM are taken as the theoretical value to analyze the calculation error of transient thermal network.

However, the surface temperature of the busbar is not uniform in the circumferential direction as seen in Fig. 5.

The maximum surface temperature difference can reach over 7 K due to the solar radiation. Moreover, the surface temperature is not symmetric because of uneven solar heat flux absorbed by the upper surface as shown in Fig. 4.

Obviously, it is difficult to obtain the average surface temperature using only one measuring point. To reduce the measurement error, a common practice is to take the arithmetic average value of multiple temperature sensors evenly attached on the surface. Let us consider n measuring points with the starting angle θin Fig. 4 and thus the average surface temperature $T_{\mathrm{sa}}(\theta)$ can be expressed as

$$T_{\mathrm{sa}}(\theta) = \sum_{i=0}^{n} T_s(\theta + 360° \times i/n)/n \qquad (13)$$

where $T_{\mathrm{s}}(\theta)$ represents the surface temperature of angle θ.

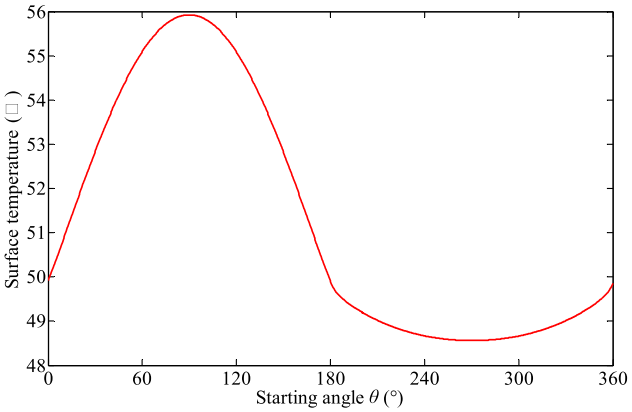

FIGURE 5. Steady-state busbar surface temperature obtained by FEM.

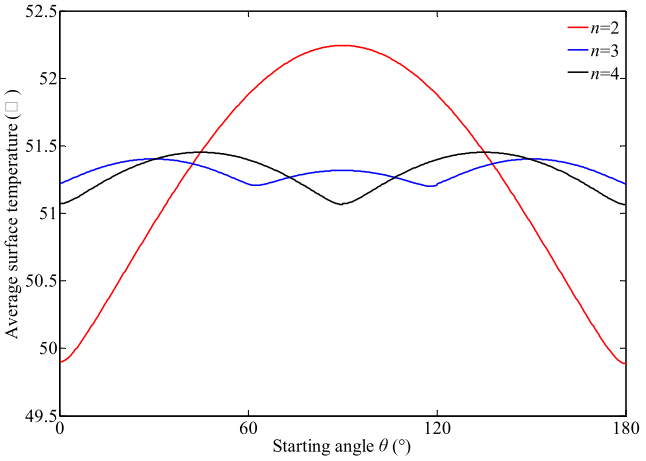

FIGURE 6. The average surface temperatures with different starting angles and number of measuring spots.

Apparently, $T_{\mathrm{sa}}(\theta)$ is related to the starting angle θ. Since X-axis is defined to be perpendicular to the sunlight, the starting angle θ changes over time and is dependent on the position of the busbar in practice. That is to say, the starting angle $\theta$is a random number. If the average temperature $T_{\mathrm{sa}}(\theta)$ changes significantly with θ, this method will be unsuitable for practical engineering. Fig. 6 shows the average surface temperatures with different starting angle θ and number of measuring points n. This result demonstrates that three temperature sensors are adequate to measure the average surface temperature of the insulated busbar with temperature difference less than 0.3 K regardless of the starting angle.

In this section, the average surface temperature used for thermal network is obtained from the FEM result with the starting angle $\theta = 0°$. The conductor temperatures obtained from transient thermal network and FEM are illustrated in Fig. 7 for comparison. It can be seen that the calculation temperature based on transient thermal network agrees well with the FEM-based result. The solar radiation effect on RDTC can be efficiently overcome by the use of the average surface temperature obtained from three temperature points evenly placed around the busbar surface.

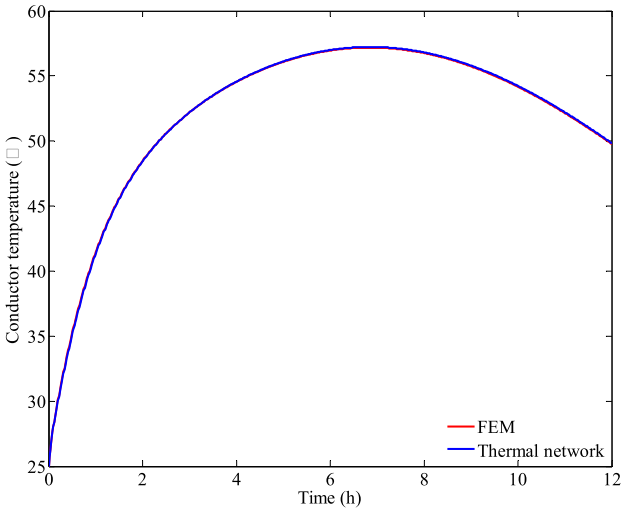

FIGURE 7. Copper conductor temperature rises of the insulated busbar without the joint calculated by thermal network and FEM.

B. ADTC

1) BASIC PRINCIPLE

As mentioned before, ADTC is utilized to estimate the hotspot temperature T_0 inside the joint from the conductor temperatures (T_1, T_2) in the busbar obtained from RDTC. Apparently, it is inconvenient to calculate T_0 by means of thermal network like RDTC, especially for the prefabricated joint, where the natural convection occurs.

Fortunately, the thermal conductivity of the conductor is considerably high and it could be expected that there is a clear correspondence between the hotspot temperature and the conductor temperatures in busbar. This correspondence can be expressed as the following functional relationship

$$T_0 = f(T_1, T_2) \tag{14}$$

The fitting samples are all extracted from the FEM-based transient thermal analysis of the insulated busbar taped joint. In consideration of the current effect, multiple thermal analyses are conducted out under single-step load currents ranging from 100 A to the rated current. In all the simulations, the hotspot temperature T_0 inside the joint and conductor temperatures (T_1, T_2) in the busbar are extracted every 1 min to constitute the overall fitting samples. Afterwards, a proper function form should be selected to determine the final expression of formula (14).

2) THE EFFECT OF SOLAR RADIATION ON CONDUCTOR TEMPERATURES

The above analysis does not take into consideration the solar radiation effect, which will in fact increase the conductor temperatures and thus change formula (14).

For this reason, this part focuses on the effect of solar radiation on the conductor temperatures through FEM.

The insulated busbar taped joint is depicted in Fig. 8 and its thermal properties are also given in Table 1. The Steel hoop is used to increase the pressure between Copper connector and the conductor for a better electrical connection. The equivalent resistance between the Copper connector and the conductor was measured to be 1.5 $\mu\Omega$ through Micro-Ohm Meter after the electric connection was finished during the assembly of a practical joint. The other boundary conditions and load current are assumed to be the same as that utilized in RDTC section.

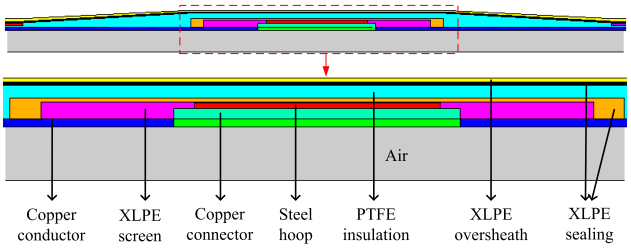

FIGURE 8. The model of the insulated busbar taped joint.

When the busbar is not subject to solar radiation, the thermal analysis can be easily conducted by a 2-D axisymmetric model, which contains joint and its adjacent busbars with the length of 5 m for axial heat flux to be zero. But while considering the solar radiation effect, a 3-D model must be resorted to. After solving the two transient thermal fields mentioned above, it is easy to obtain the temperature rise caused by the solar radiation, which equals the temperature difference between these two models.

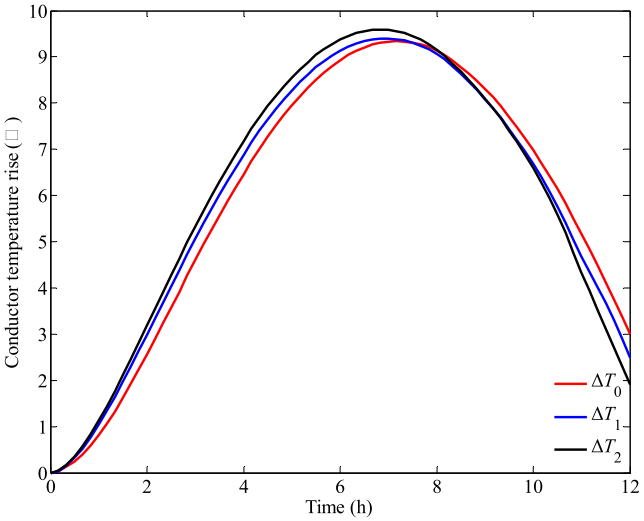

FIGURE 9. Conductor temperature rises caused by solar radiation.

The distances between measuring spot 1, 2 in the conductor and the end of joint are assumed to be 0.2 m and 2.2 m, respectively. The conductor temperature rises ΔT_0, ΔT_1 andΔT_2 caused by solar radiation are shown in Fig. 9. It can be seen that the conductor temperature rises due to the solar radiation in either the joint or busbar are almost the same with the maximum difference of about 1 K. Thus, the solar radiation effect can be equivalent to an identical increment ΔT in all the conductor temperatures.

3) THE SELECTION AND DETERMINATION OF FORMULA (14)

Formula (14) should satisfy the following constraints in the sunlight according to the previous analysis.

$$T_0 + \Delta T \equiv f(T_1 + \Delta T, T_2 + \Delta T) \tag{15}$$

On the basis of Taylor's theorem, the expression on the right side of formula (15) can be expanded as follows.

$$\begin{aligned} &f(T_1 + \Delta T, T_2 + \Delta T) \\ &\quad = f(T_1, T_2) + (\Delta T \frac{\partial}{\partial T_1} + \Delta T \frac{\partial}{\partial T_2}) f(T_1, T_2) \\ &\qquad + \frac{1}{2!}(\Delta T \frac{\partial}{\partial T_1} + \Delta T \frac{\partial}{\partial T_2})^2 f(T_1, T_2) + \ldots\ldots \end{aligned} \tag{16}$$

where

$$(\Delta T \frac{\partial}{\partial T_1} + \Delta T \frac{\partial}{\partial T_2})^m f(T_1, T_2) = \sum_{i=0}^{m} C_m^i \frac{\partial^m f}{\partial x^i \partial y^{m-i}} \cdot \Delta T^m$$

By combining formula (14), formula (15), and formula (16), those formulae can be simplified as

$$\Delta T \equiv \Delta T \frac{\partial f}{\partial T_1} + \Delta T \frac{\partial f}{\partial T_2} + \frac{1}{2!} \sum_{i=0}^{2} C_2^i \frac{\partial^2 f}{\partial x^i \partial y^{2-i}} \cdot \Delta T^2 + \ldots\ldots \tag{17}$$

In order to make the above formula constant, the quadratic and higher order coefficients must be equivalent to zero, namely

$$\sum_{i=0}^{m} C_m^i \frac{\partial^m f}{\partial x^i \partial y^{m-i}} \equiv 0 \quad m \geq 2 \tag{18}$$

In the light of Taylor series, any function can be expressed as the sum of polynomials. Apparently, only when all high order ($\geq$2) coefficients of the function f are equal to zero can equations (18) be constantly satisfied. That is to say, the function f must be a linear function, which can be expressed as follows

$$f(T_1, T_2) = aT_1 + bT_2 + c \tag{19}$$

where a, b and c are all undetermined constants. By substituting formula (19) into formula (15), one can acquire the following formula

$$\begin{aligned} T_0 + \Delta T &= a(T_1 + \Delta T) + b(T_2 + \Delta T) + c \\ &= aT_1 + bT_2 + c + (a + b)\Delta T \\ &= f(T_1, T_2) + (a + b)\Delta T \end{aligned} \tag{20}$$

Combining the above formula and formula (14), the following constraints can be readily obtained

$$a + b = 1 \tag{21}$$

Thus, the final form of the function can be written as follows

$$f(T_1, T_2) = aT_1 + (1 - a)T_2 + c \tag{22}$$

Apparently, the above function form is based on two fixed measuring spots in the conductor. For the sake of parameter optimization, it is necessary to discuss the effect of the number and location of measuring spots in the busbar. Similar to formula (22), the general function form of ADTC with multiple measuring spots can be written as

$$f(T_1, \ldots, T_n) = \sum_{i=1}^{n-1} a_i T_i + (1 - \sum_{i=1}^{n-1} a_i) T_n + c \tag{23}$$

If only one measuring spot is selected, the first-order coefficient a on the right side of the formula (23) is equal to one and the unique undetermined coefficient is c. In this case, however, c is not a constant at all. For example, when the load current is zero, the steady-state temperature of the busbar is the ambient temperature, which means that c should be equal to zero. In the other situations, c is always a positive number depending on the current because the hotspot temperature T_0 in the joint is clearly higher than the conductor temperature in the busbar. That is to say, only one measuring spot in the busbar is insufficient to calculate the hotspot temperature using our approach.

In order to evaluate the performance of ADTI with multiple spots, two assessment indexes are introduced in this paper. The first one is the coefficient of determination R^2 used to quantify the accuracy of the data fitting. The second one is the maximum absolute value of first-order coefficient, which is $\max|a_i|$ in formula (23), to estimate the anti-disturbance capacity of ADTI. This is because that the input of ADTI is the output of RDTI so that the calculated error of T_i from RDTI will be magnified by a factor of $|a_i|$ in the ADTI. Obviously, a higher value of maximum absolute value of first-order coefficient indicates a more sensitive thermal response to the temperature disturbances together with a worse robust performance of ADTI and vice versa.

To determine the number and location of measuring spots in the busbar, five fixed spots were selected in the conductor of the busbar with the corresponding conductor temperatures named T_{c1}, T_{c2}, T_{c3}, T_{c4} and T_{c5}. The distances between these points and the joint end are set to 0.2 m, 0.3 m, 0.45 m, 0.7 m and 2.2 m respectively so that these temperatures are nearly an arithmetic progression outlining the rough temperature distribution of the conductor. All these temperatures are extracted from the FEM-based transient thermal analysis as described in ''Methodology B.1)'' section. The formula (23) is adopted for the data fitting in ADTI with different measuring spots combining together. There are totally 26 possible combinations from five spots and each combination can constitute an independent and complete ADTI.

It is found that the coefficients of determination of data fittings are all over 0.99, but the maximum absolute values of first-order coefficient, as shown in Table 3, differ from each other. In this table, a_{123} means the maximum absolute value of first-order coefficient using T_{c1}, T_{c2} and T_{c3} and the others can be understood similarly. Two main conclusions can be intuitively obtained from this table. The first one is that the

TABLE 3. The maximum absolute values of first-order coefficient with different measuring spots combination.

a_{12}	a_{13}	a_{14}	a_{15}	a_{23}	a_{24}	a_{25}	a_{34}	a_{35}
11.7	6.1	4.4	3.5	11.8	6.5	4.6	13.0	6.9
a_{45}	a_{123}	a_{124}	a_{125}	a_{134}	a_{135}	a_{145}	a_{234}	a_{235}
13.5	99.2	48.1	27.7	40.2	16.5	16.1	77.8	32.0
a_{245}	a_{345}	a_{1234}	a_{1235}	a_{1245}	a_{1345}	a_{2345}	a_{12345}	
23.4	45.33	451	233	106	103	193	510	

maximum absolute values of first-order coefficient with three or more measuring spots are quite large while those with two measuring spots are relatively much lower. The second one is that in the case of only two measuring spots, the greater the distance between the measuring spots, the lower their maximum absolute values of first-order coefficient. It can be observed that a_{15} is the minimum according to this table. Thus it is recommended that ADTI needs only two measuring spots in the busbar, with one spot adjacent to the joint end and the other one sufficiently distant from the joint to be thermally independently of it. Based on the above analysis, the formula (22) is the optimal function form for data fitting in ADTI.

The formula (22) is essentially the combination of formula (14) and formula (15), That is to say, even if the training samples used for fitting formula (22) come from the thermal analyses where no solar radiation is applied, the fitted formula is also suitable for a busbar joint that is exposed to the sun.

For better understanding of the above statement, let us assume that T_1 and T_2 are the conductor temperatures without considering the solar radiation effect. When the busbar is exposed to the sun, all the conductor temperatures in the busbar will have almost an identical increment ΔT as analyzed before. In this case, the temperature inside the joint estimated using formula (22) is as follows

$$\begin{aligned} &f(T_1+\Delta T, T_2+\Delta T) \\ &\quad = a(T_1+\Delta T)+(1-a)(T_2+\Delta T)+c \\ &\quad = aT_1+(1-a)T_2+c+\Delta T = f(T_1,T_2)+\Delta T \end{aligned} \tag{24}$$

This formula implies that the temperature rise ΔT in both T_1 and T_2 caused by the solar radiation will also give rise to a same temperature rise ΔT in the estimated temperature inside the joint. As mentioned in ''Methodology B.2)'' section, all the conductor temperatures, including the hotspot temperature inside the joint, will increase by approximately ΔT. Consequently, the estimated temperature can always be deemed as a good approximation of the real temperature inside the joint, no matter how the solar radiation changes.

To sum up, the final expression of formula (22) in ADTC can be derived through the following steps:

Step 1: Perform transient FEM thermal analysis of the insulated busbar taped joint under single-step load current of 100 A. The boundary conditions are based on formula (9)-(12). After completing the solution, extract the hotspot temperature T_0 inside the joint and conductor temperatures (T_1, T_2) in busbar every 1 min.

Step 2: Repeat the above thermal analyses with single-step currents of 200 A, 300 A, 400 A …, 1300 A and then extract the temperatures the same as those in Step 1. All of those extracted temperature data constitute the entire training samples.

Step 3: Fit formula (22) by the use of the above training samples and then the final functional expression is calculated as follows

$$T_0 = f(T_1, T_2) = 3.521T_1 - 2.521T_2 + 0.0006 \tag{25}$$

For comparison, the functional expression based on formula (19), which does not consider the solar radiation effect, is also given as follows

$$T_0 = f(T_1, T_2) = 1.6481T_1 - 0.4357T_2 - 5.4036 \tag{26}$$

It should be noted that one approximation function from the FEM calculation cannot be valid for all types of joints and their initial joint resistances. This is because that the fitting samples all come from the thermal analyses, which are clearly dependent upon the structure and thermal parameters of the object, including the joint types and their contact resistances. For this reason, in practical applications, it is necessary to perform thermal analyses for each type of joints to obtain their corresponding approximation functions. It is also recommended to measure the initial contact resistance during the assembly of joint to build a more accurate calculation model for the approximation function in ADTC.

III. TEST ARRANGEMENT

In order to verify the validity of the proposed approach, this paper conducted the temperature-rise test on a practical insulated busbar taped joint in the outdoors. The dimension and material of this object are identical to that described in Methodology section.

A. GENERAL OVERVIEW

The test arrangement is illustrated in Fig. 10. As seen from these figures, four separate busbar segments were connected together to form a rectangular test loop through Copper bus, inducing transformer and two taped joints. The metering class current transformer was connected to a data logger for collecting the current generated by inducing transformer. The length of each busbar element is 5 m to ensure that the temperatures of joints and surface temperature measuring spots are unaffected by the end of the busbar.

The Platinum resistance thermometers with tolerance class of A [35] were selected for temperature measurement. The distances between surface temperature measuring spots and the joint end were 0.2 m and 2.2 m; three sensors were evenly attached on the surface for each measuring spot, which is consistent with the previous analysis. To reduce the impact of the surrounding environment on the surface temperature

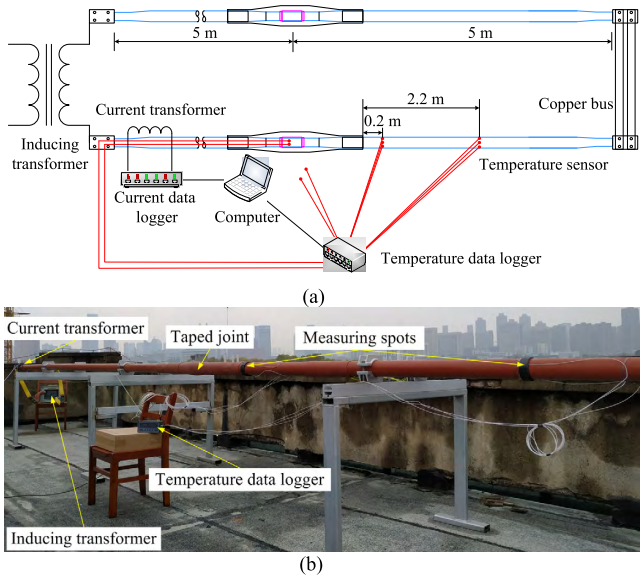

FIGURE 10. The test arrangement. (a) Schematic diagram, (b) Photo.

measurement, each measuring spot was covered by a rubber tube with the width of 3 cm and thickness of 4 mm. Another two temperature sensors were placed in air to obtain the ambient temperature near the taped joint. Besides, since the circuit was not energized, two more sensors were inserted into the joint for hotspot temperature measurement, which will be described in detail in the following passage.

B. THE ASSEMBLY OF THE INSULATED BUSBAR TAPED JOINT

A common practice for temperature measurement in the joint is to put thermometers on the outer surface of the connector [14]. In this situation, the lead wire of thermometer will be sandwiched between the joint and the busbar, thus changing the structure and temperature profile of the original joint. This paper cleverly utilizes the hollow structure of the busbar to achieve temperature measurement without affecting the original structure of the taped joint.

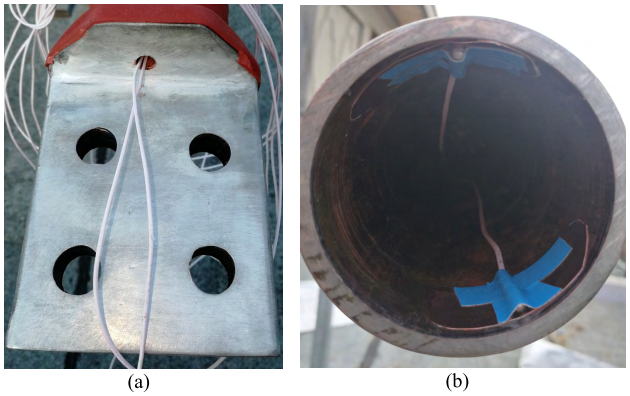

FIGURE 11. Arrangement of thermometers for hotspot temperature measurement. (a) Drilling a hole on the terminal, (b) Fixing sensors on the inner surface.

As shown in Fig. 11(a), a hole was drilled on the flat terminal on one end of the insulated busbar for two thermometers to pass through. Afterwards, the two sensors were pushed out of the other end of the busbar where a joint would be installed. Finally the sensors were bonded to Copper sheets with thermally conductive adhesive tape, and fixed to the inner surface of the conductor with thermally conductive grease as seen in Fig. 11(b). Since the thermometers were attached on the inner surface, the structure of the joint as well as the temperature distribution was not affected.

The first step of joint assembly is the electrical connection between two conductors. In Fig. 12(a), the end of conductor on the right side was designed into a connector with four petals that were prised to cover the conductor on the left side. In order to increase the contact pressure between the connector and conductor, a cylindrical Steel hoop, which is always a part of the joint, was utilized to clamp the outer surface of connector, as shown in Fig. 12(b).

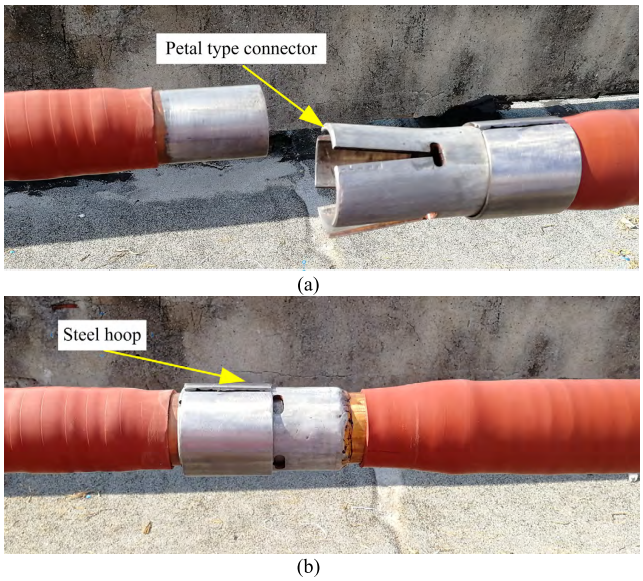

FIGURE 12. The connection method of the conductors. (a) Prise the petal type connector, (b) Clamp the connector using Steel hoop.

After connecting the conductors, the conductor screen, sealing, PTFE insulation and so on were successively wrapped on the joint according to Fig. 8 for the insulating and waterproof purpose as seen in Fig. 13.

IV. RESULTS

The temperature-rise test was performed in Wuhan University at the beginning of August with the strongest solar radiation in a year. The test results and the calculated hotspot temperatures based on RDTC and ADTC are shown in Fig. 14. The first graph shows the change of conductor current with time and the second graph illustrates the measured and calculated hotspot temperatures and ambient temperature. The last graph represents the temperature errors between the measured temperature and calculated ones. All of the collected data were recorded every 1 min and for comparison both formula (25)

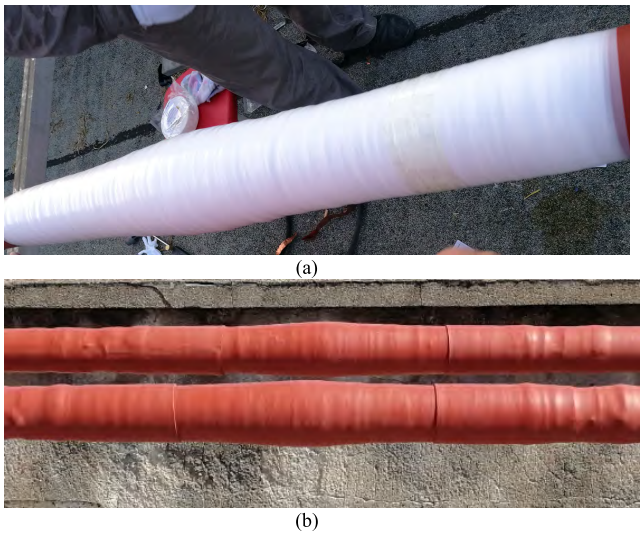

FIGURE 13. The insulation and waterproof treatment of the joint. (a) Wrap the PTFE insulation, (b) Shrink the oversheath.

and formula (26) of ADTC are used to estimate the hotspot temperature in this figure. During the test, the ambient temperature ranged from 25 to 40° and the load current varied between 0 and 1350 A.

According to this figure, the calculated temperature based on formula (26) is obviously larger in the daylight with maximum error of about 7 K whereas that of formula (25) is much closer to the measured result with error less than 3.8 K. It can also be found from the error curves that the temperature obtained from formula (25) is nearly an unbiased estimate of the measured value with the average error of 0.55 K. Moreover, when the conductor temperature reached the maximum, about 74 °C, the calculated temperature error is quite small. This point is essentially important because during the temperature monitoring it is the maximum temperature that really matters. Thus, the accuracy of the presented approach based on formula (25) is always high, especially for conductor temperature over 70 °C, regardless of varying load current, ambient temperature and solar radiation, meeting the requirements for engineering application. On the other hand, the overall temperature based on formula (26) is larger than the measured result of which the mean error is nearly 2.5 K. The result indicates that the proposed approach based on formula (25) is suitable for temperature monitoring for the insulated busbar joint considering the solar radiation effects.

A. DISCUSSIONS

1) THE FUNCTION OF COVER ON THE SURFACE TEMPERATURE MEASUREMENT

The proposed model requires two inputs, namely current and two surface temperatures. The former one can be accurately obtained by current transformer while special attention should be paid to the latter ones.

If the temperature sensor is directly laid on the busbar surface without any cover, the temperature sensor will absorb

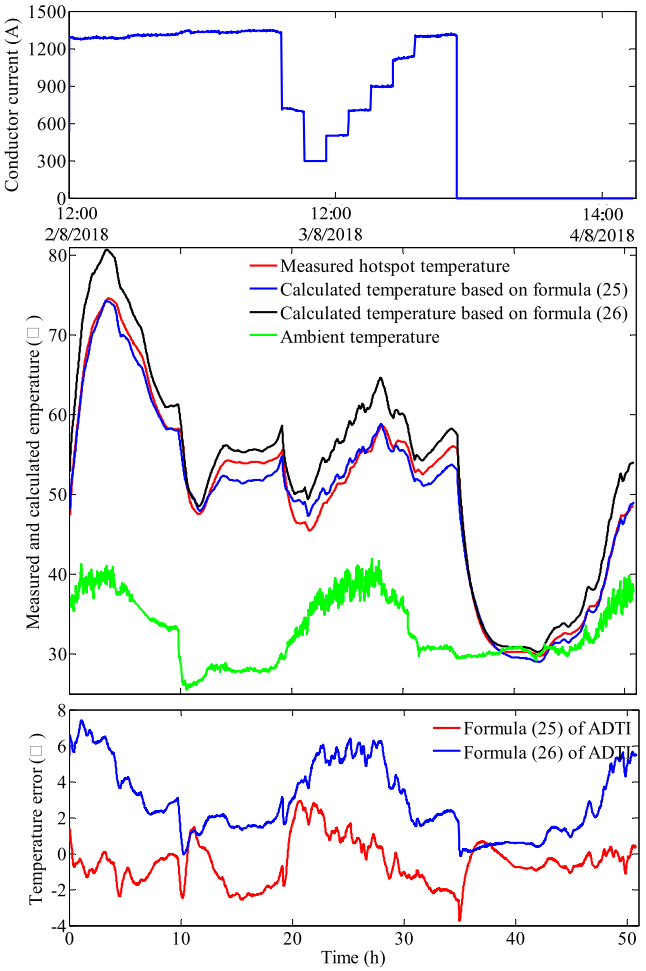

FIGURE 14. The measured results and calculated hotspot temperatures.

the heat from the surface while dissipating heat into the surrounding air. That is to say, the temperature measured by the sensor will be between the real surface temperature and the ambient temperature. For a better understanding, let us perform a steady-state 3-D thermal analysis. The structure of the fully insulated busbar is identical to that in Fig. 2 with the length of 1 m. The sensor is modeled as a cylinder with the height of 2 cm and diameter of 2.5 mm. The busbar surface and the sensor are tangent to simulate the mutual contact.

The resistance thermometer usually consists of Platinum wire, a ceramic mandrel (in most cases Alumina) and a metal protective sheath [36] . Since the wire and sheath are quite thin, the thermal conductivity of the whole resistance thermometer can be regarded as that of Alumina, which is about 30 W/(m·K) [37] . The heat source and boundary conditions are the same as those in the preceding passage except that the solar radiation is not applied so as to reveal the measurement error at night, when the temperature difference between the surface and surrounding is less noticeable. The steady-state temperature profile is depicted in the blue part of Fig. 15. The temperature in the sensor is clearly lower than neighboring surface temperature, and the difference between real surface temperature and the measured one is over 5 K. This is because

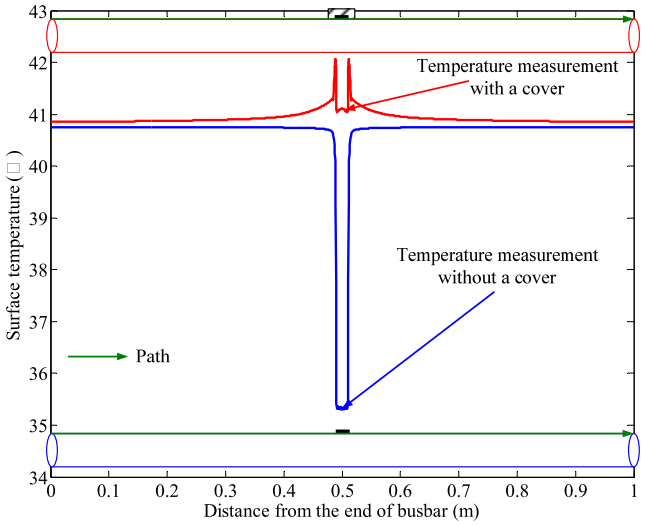

FIGURE 15. The axial surface temperatures along the paths passing the temperature sensor with or without a cover.

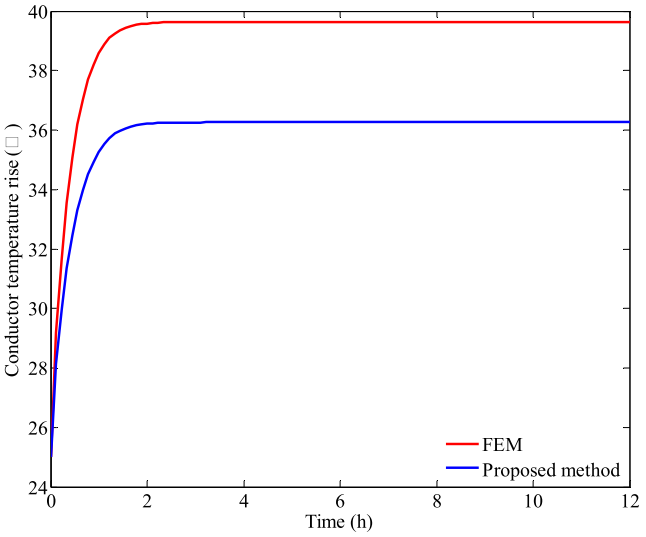

FIGURE 16. The conductor temperature rises obtained by FEM and the proposed method considering the rain effect.

that most part of the sensor is exposed to the air, which is equivalent to increasing the local surface area of the busbar, causing a significant temperature drop.

To avoid the aforementioned measurement error, the temperature sensor is covered by a rubber tube with width of 3 cm and thickness of 4 mm to prevent the heat from being dissipated to the surrounding air. The thermal conductivity of rubber tube is nearly 0.035 W/(m·K). The simulation results are sketched in the red line of Fig. 15. It can be found that the temperature difference between the real surface temperature and measured value is considerably lower. This comparison strongly illustrates the role of the cover in improving the measurement accuracy of surface temperature.

2) THE EFFECT OF RAIN ON THE PROPOSED METHOD

Except for solar radiation, the busbars are also affected by wind and rain in practice. Unlike the solar radiation, both wind and rain are equivalent to enhancing the heat dissipation between the surface and the surroundings. In this part, the FEM thermal analysis is utilized to simulate their effects on our approach. Since the cooling capacity of water is much stronger than that of water, only the rain effect is considered here.

The solar radiation can be obviously ignored in a rainy day. Furthermore, the convective heat transfer coefficient of water is so large that the surface temperature can be taken as the ambient temperature. In the simulation, both the ambient temperature and the initial temperature of the insulated busbar are all set to 25°. When $t > 0$, a current of 1300 A is injected into the conductor in a rainy day. After solving the transient temperature field, collect the temperature inside the joint and two surface temperatures of busbar. With the above surface temperatures and current, the temperature inside the joint can be estimated using the developed approach, as shown in Fig. 16. The result obtained by FEM, deemed as the theoretical value, is also provided for comparison.

It can be observed that calculated temperature by the presented method is invariably lower than the FEM result with maximum difference of 3.5 K. The underlying cause is that the functional relationship for ADTC is obtained from the thermal analyses without wind and rain. Consequently, if the convective heat transfer coefficient changes due to wind or rain, the functional relationship between hotspot temperature and conductor temperatures will also vary. Fortunately, although the proposed method cannot accurately estimate the temperature inside the joint with strong wind or heavy rain, an error of less than 4 K is usually acceptable, because in this case the conductor temperature is not sufficiently high to accelerate the insulation thermal ageing.

V. CONCLUSION

This paper develops an approach to indirectly monitor the hotspot temperature inside the fully insulated busbar taped joint from busbar surface temperatures and load current. The solar radiation effect is discussed in detail and successfully overcome theoretically and experimentally.

The temperature-rise test on a practical insulated busbar taped joint was carried out under multi-step currents outdoors in hot summer. The calculated hotspot temperature based on the proposed method is in good agreement with the measured result with maximum error of nearly 3.8 K. This demonstrates that this approach can greatly reduce the impact of solar radiation and satisfy the accuracy requirement with the busbar being directly exposed to the sun.

This paper focuses mainly on the taped joint, and future attention will be paid to validating the applicability of the presented approach on the prefabricated busbar joint.

ACKNOWLEDGMENT

The authors would like to thank Hubei Xinghe Electric Power New Material Co., Ltd., who provided and assembled the fully insulated busbar taped joint.

REFERENCES

[1] *Busbar System with ERIP-Insulation for Medium Voltage*. Accessed: May 26, 2019. [Online]. Available: http://pbp-preissinger.de/en/product/isobus-mr

[2] *Product Overview of Duresca Busbar System*. Accessed: May 26, 2019. [Online]. Available: http://www.mgc.ch/fileadmin/user_upload/MGC_180122_DURESCA_Stromschienen-e_WEB.pdf

[3] *SIS Solid Insulation System*. Accessed: May 26, 2019. [Online]. Available: http://ritz-international.com/wp-content/uploads/2015/12/RITZ-SIS_Solid-Insulation_System_ENG_Rev_2013-10.pdf

[4] R. Worth, M. Islam, and C. Smith, "Insulated bus pipe (IBP) for power utility applications," in *Proc. IEEE 11th Int. Conf. Transmiss. Distrib. Construct., Operation Live-Line Maintenance*, Oct. 2006, pp. 1–5.

[5] M. Islam, R. Worth, and C. Smith, "Insulated bus pipe (IBP) for shipboard application," in *Proc. 53rd IEEE Ind. Appl. Soc. Annu. Petroleum Chem. Ind. Conf.*, Sep. 2006, pp. 1–6.

[6] R. Worth, M. Islam, R. H. Pater, and C. Smith, "Insulated bus pipe (IBP) for shipboard applications," in *Proc. IEEE Elect. Ship Technol. Symp.*, May 2007, pp. 122–129.

[7] S. W. Li, N. Wang, J. F. Guo, J. J. Zan, Y. Gao, S. H. Huang, and B. X. Du, "Effect of thermal ageing on electrical and mechanical properties of tubular bus model insulation," in *Proc. IEEE Int. Conf. High Voltage Eng. Appl.*, Sep. 2016, pp. 1–4.

[8] *China Electricity Council*. Accessed: May 26, 2019. [Online]. Available: http://dls.cec.org.cn/yijianzhengqiu/2015-05-08/137538.html

[9] Z. Sirui, R. Ling, R. Xiang, L. Wenpei, and X. Bin, "Research on the defects in the field installation of insulated tubular bus-bar and its test method," in *Proc. 20th Int. Conf. Elect. Mach. Syst.*, Aug. 2017, pp. 1–5.

[10] J. Liao *et al.*, "Fault analysis and treatment of insulated bus bar in TCR branch of DC deicer and SVC," *Electr. Wire Cable*, no. 6, pp. 41–44, Dec. 2017.

[11] J. N. Zhang, X. B. Huang, and L. X. Liang, "Engineering application of insulated tube busbar to half insulated tube busbar," *Electr. Wire Cable*, no. 3, pp. 42–44, Jun. 2018.

[12] L. Ruan *et al.*, "Development status and research trend of insulated tubular bus," *High Voltage App.*, vol. 54, no. 4, pp. 43–53, Apr. 2018.

[13] F. Liu, Z. Xue, Y. Deng, and Q. Ma, "Operating characteristics and state evaluation methods for insulated tubular bus-bar," *High Voltage Eng.*, vol. 43, no. 12, pp. 4088–4095, Dec. 2017.

[14] Z. Zhen-Peng, R. Wenbin, R. Ling, Z. Jian-Kang, M. Shao-Xin, and Y. Fan, "Research on the temperature rise characteristic of 10 kV fully insulated busbar system," in *Proc. China Int. Conf. Elect. Distrib. (CICED)*, Aug. 2016, pp. 1–4.

[15] J. Ma *et al.*, "Technical and economic benefit evaluation for medium voltage compact insulated tube type bus conductor," *Guangdong Elect. Power*, vol. 31, no. 6, pp. 32–39, Jun. 2018.

[16] Y. H. Zheng, Q. B. Wu, H. Q. He, and M. H. Wang, "Detecting and diagnosis of partial discharge in a fully insulated pipe type bus bar," *Insulating Mater.*, vol. 43, no. 4, pp. 63–66, Apr. 2010.

[17] P. H. Li, L. Ruan, C. L. Li, F. Yang, H. Y. Jin, and S. R. Zhu, "Optimization for epoxy/paper composites insulated tubular bus structure," *Mater. Sci. Forum*, vol. 922, pp. 169–174, May 2018.

[18] X. H. Zhang, F. Liu, Y. Deng, D. Ding, Q. Ma, and S. Fan, "Analysis on abnormal operation and structure of a 35 kV insulating tubular bus bar," *High Voltage App.*, vol. 52, no. 1, pp. 190–197, Jan. 2016.

[19] L. Li, X. Yu, and Z. H. Tong, "Review and prospect of the organic insulated bus in China," *High Voltage App.*, vol. 52, no. 6, pp. 9–17, Jun. 2016.

[20] L. Zhang, J. F. Liang, X. Hou, Y. Gao, and J. Li, "The partial discharge characteristics study of insulated copper bus bar," in *Proc. Annu. Rep. Conf. Elect. Insul. Dielect. Phenomena*, Oct. 2013, pp. 1169–1172.

[21] Y. Gao, L. Y. Chen, L. M. Zhang, S. H. Huang, B. X. Du, and F. Wang, "PD characteristics in PTFE insulated tubular busbar models measured with HFCT and acoustic sensor," in *Proc. IEEE 11th Int. Conf. Properties Appl. Dielect. Mater. (ICPADM)*, Jul. 2015, pp. 736–739.

[22] X. M. Hu, L. X. Liang, Z. R. Tan, L. Zhang, J. H. Li, and Y. M. Li, "The partial discharge characteristics study of the insulated copper busbar joint metal metal protrusion defect," *Adv. Mater. Res.*, vol. 614, pp. 1126–1130, Dec. 2013.

[23] F. Liu, Z. Xue, Y. Deng, Q. Ma, Y. Liu, C. Wu, W. Li, and J. Zhu, "Researches on abnormal operating and condition assessment methods for insulating tubular bus-bar," in *Proc. Int. Conf. Condition Monit. Diagnosis (CMD)*, Sep. 2016, pp. 110–113.

[24] L. Zhang, J. H. Li, J. Y. Tan, X. M. Hu, Y. M. Li, and Z. R. Tan, "Characteristics of surface partial discharge on joint of insulated copper busbar," *High Voltage App.*, vol. 49, no. 11, pp. 94–98, Nov. 2013.

[25] C. L. Li, R. Liu, P. H. Li, W. P. Li, and N. K. Gao, "Electric field simulation of typical defects in the epoxy/paper composites insulated tubular bus," *Mater. Sci. Forum*, vol. 922, pp. 157–162, May 2018.

[26] L. Wenpei, R. Xiang, R. Ling, and Z. Sirui, "Simulation of the effect of bubble defect on the distribution of electric field in epoxy resin pouring type insulated tubular bus-bar," in *Proc. 20th Int. Conf. Elect. Mach. Syst. (ICEMS)*, Aug. 2017, pp. 1–5.

[27] L. M. Zhang *et al.*, "Effect of thermal ageing on properties of PET films as novel insulating material for tubular bus," *Insulating Mater.*, vol. 49, no. 8, pp. 44–48, Aug. 2016.

[28] J. J. Ruan, C. Liu, D. C. Huang, Q. H. Zhan, and L. Z. Tang, "Hot spot temperature inversion for the single-core power cable joint," *Appl. Therm. Eng.*, vol. 104, pp. 146–152, Jul. 2016.

[29] *IEC Standard-Calculation of the Cyclic and Emergency Current Rating of Cables—Part 2: Cyclic Rating of Cables Greater Than 18/30 (36) kV and Emergency Ratings for Cables of All Voltages*, IEC Standard 60583-2, 1989.

[30] D. M. Price and M. Jarratt, "Thermal conductivity of PTFE and PTFE composites," *Thermochimica Acta*, vol. 392, pp. 231–236, Sep. 2002.

[31] J. Blumm, A. Lindemann, M. Meyer, and C. Strasser, "Characterization of PTFE using advanced thermal analysis techniques," *Int. J. Thermophys.*, vol. 31, no. 10, pp. 1919–1927, Oct. 2010.

[32] Y. A. Cengel, *Introduction to Thermodynamics and Heat Transfer*. New York, NY, USA: McGraw-Hill, 2008.

[33] *IEC Standard-Electric Cables- Calculation of the Current Rating—Part 1-1: Current Rating Equations (100 Load Factor) and Calculation of Losses-General*, IEC Standard 60287-2, 2006.

[34] M. R. Tanaskovic, "Calculation of the ampacity of high voltage cables laid in free air," *Tehnika*, vol. 73, no. 1, pp. 89–98, Dec. 2018.

[35] *Industrial Platinum Resistance Thermometers and Platinum Temperature Sensors*, IEC Standard 60751, 2016.

[36] W. L. Brown, "Electrical resistance element," U.S. Patent 3 694 789, Sep. 26, 1972.

[37] *Aluminium Oxide*. Accessed: May 26, 2019. [Online]. Available: https://en.wikipedia.org/wiki/Aluminium_oxide

LIEZHENG TANG was born in Beijing, China, in 1993. He received the B.S. degree in electrical engineering and automation from the School of Electrical Engineering and Automation, Wuhan University, Wuhan, China, in 2015, where he is currently pursuing the Ph.D. degree in electrical engineering. His research interests include condition monitoring, and the insulation design of the cable joint and dielectric breakdown voltage prediction.

JIANGJUN RUAN was born in Zhejiang, China, in 1968. He received the B.S. and Ph.D. degrees in electric machine engineering from the Huazhong University of Science and Technology, Wuhan, China, in 1990 and 1995, respectively. He was a Postdoctoral Researcher from the Wuhan University of Hydraulic and Electric Engineering, Wuhan, in 1998. He is currently a Professor with the School of Electrical Engineering and Automation, Wuhan University. His research interests include electromagnetic field numerical simulation, high voltage, and insulation technology.

ZHIFEI YANG was born in Henan, China, in 1990. He is currently pursuing the Ph.D. degree in electrical engineering from the School of Electrical Engineering and Automation, Wuhan University, Wuhan, China. His research interests include the numerical calculation of electromagnetic field, high voltage, and insulation technology.

ROU CHEN was born in Hubei, China, in 1993. She received the master's degree in electrical engineering from the School of Electrical Engineering and Automation, Wuhan University, Wuhan, China, in 2018. She is currently with China Electric Power Research Institute Co., Ltd., Wuhan, China. Her research interests include the numerical calculation of electromagnetic field, high voltage, and insulation technology.

GUANNAN LI was born in Sichuan, China, in 1994. He received the B.S. degree in electrical engineering and automation from the School of Electrical Engineering and Automation, Wuhan University, Wuhan, China, in 2017, where he is currently pursuing the master's degree in electrical engineering. His research interests include the numerical calculation of electromagnetic field, high voltage, and insulation technology.

XUEFENG YIN was born in Jiangxi, China, in 1996. He is currently pursuing the master's degree in electrical engineering from the School of Electrical Engineering and Automation, Wuhan University, Wuhan, China. His research interests include thermal analysis, high voltage, and insulation technology.